

# Simulation-Based Optimization of Figure-of-Eight Coil Designs and Orientations for Magnetic Stimulation of Peripheral Nerve

Pragya Kosta<sup>1</sup>, Member, IEEE, John Mize<sup>2</sup>, David J. Warren<sup>3</sup>, Senior Member, IEEE, and Gianluca Lazzi, Fellow, IEEE

**Abstract**—Although magnetic neural stimulation has many advantages over electrical neural stimulation, its main disadvantages are higher energy requirement and poor stimulation selectivity. The orientation and location of the coil with respect to the stimulation site play a critical role in determining the stimulation threshold and stimulation selectivity. Utilizing numerical simulations in this work, we optimized the design parameters, orientation, and positioning of magnetic coils with respect to the peripheral nerve for improved stimulation efficacy. Specifically, we investigated different orientations and positions of the figure-of-eight coils for neural stimulation of the rat sciatic nerve. We also examined the effect of coil design parameters (number of layers and turns) and different coil electrical configurations (opposite vs. same direction of coil currents and series vs. parallel coil connections) on the stimulation threshold. We leveraged the multi-resolution impedance method and a heterogeneous multi-fascicular anatomical model of rat sciatic nerve to explore the possibility of selective stimulation as well. Neural excitation of a nerve fiber was implemented by an equivalent cable model and Frankenhaeuser-Huxley equations using NEURON software. Results suggest that inter-fascicular selectivity could be achieved by properly orienting and positioning the coil with respect to the nerve. Further, by orienting the figure-of-eight coil at an angle of 90° and 6 mm offset, we could switch between primarily activating one fascicle (and barely activating the other) and reversing those roles by merely switching the current direction in the two coils of the figure-of-eight coil.

**Index Terms**—Magnetic stimulation, peripheral nerve stimulation, figure-of-eight coils, coil orientations, selectivity.

## I. INTRODUCTION

ONE of the prime challenges of electrical neural stimulation is to create ideal contact between the excitable tissue and the stimulating electrode. The charge deposition at the tissue-electrode interface and foreign body reaction can result in electrode corrosion, degraded stimulation performance, deleterious immune response, and potential tissue damage over time [1], [2]. Magnetic neural stimulation overcomes these problems by providing stimulation via magnetic fields from coils enclosed in bio-compatible packaging, thereby avoid the chemical reactions that take place at the tissue-electrode interface. Further, as the biological tissue has almost uniform relative permeability, the distribution of the magnetic fields is not differentially affected by tissue heterogeneity. Therefore, in the case of magnetic stimulation, the induced current can be altered with relative ease, compared to electric stimulation in which the current follows the path of least resistance. Magnetic neural stimulation has been considered as a treatment option for both central nervous system (CNS) and peripheral nervous system (PNS) diseases, as in the case of transcranial magnetic stimulation (TMS) for treatment-resistant depression and neuropathic pain [3]–[5]. Recently, magnetic neural stimulation has been explored for sensory prostheses as well, including retinal stimulation [6] and cochlear implants [7]. However, the performance of magnetic neural stimulation is limited by two primary challenges: high energy requirements and poor stimulation selectivity [5], [8], [9]. In order to evoke a similar neural response, magnetic stimulation requires multiple orders of magnitude more energy than electrical stimulation [9]. Further, as the nerve fibers are arranged according to their association with different muscles [10], selective stimulation of desired nerve fibers (without simultaneously stimulating neighboring nerve fibers) is necessary to achieve selective muscle reanimation.

Multiple studies have been performed to enhance the performance of magnetic stimulation of CNS and PNS,

Manuscript received April 13, 2020; revised September 4, 2020; accepted November 11, 2020. Date of publication November 17, 2020; date of current version January 29, 2021. This work was supported by the National Science Foundation under Grant ECCS-1202235. (Corresponding author: Pragya Kosta.)

Pragya Kosta is with the Department of Electrical and Computer Engineering, The University of Utah, Salt Lake City, UT 84112 USA (e-mail: pragya.kosta@utah.edu).

John Mize is with the Department of Biomedical Engineering, The University of Utah, Salt Lake City, UT 84112 USA (e-mail: jack.mize@utah.edu).

David J. Warren is with the Department of Biomedical Engineering and Electrical and Computer Engineering, The University of Utah, Salt Lake City, UT 84112 USA (e-mail: david.warren@utah.edu).

Gianluca Lazzi is with the Department of Electrical and Computer Engineering, Biomedical Engineering, Ophthalmology and Clinical Entrepreneurship, University of Southern California, Los Angeles, CA 90089 USA (e-mail: lazzi@usc.edu).

Digital Object Identifier 10.1109/TNSRE.2020.3038406

with the help of novel coil designs and efficient stimulator circuits [11]–[14]. Stimulation current waveforms have been optimized to minimize the pulse energy loss, power consumption, and heating [15]–[18]. We recently proposed a current truncating stimulator circuit to reduce the stimulation energy and heat produced in the coil during the magnetic stimulation of the peripheral nerve [19]. In another work, we proposed an array of four magnetic coils to stimulate the sciatic nerve with inter-fascicular and intra-fascicular selectivity [20]. The four coils of the array are placed surrounding the nerve, and fields inside the nerve are steered by altering the coil current amplitudes and directions. The coil array could selectively stimulate three different nerve regions where nerve fibers innervate medial gastrocnemius, plantaris, and tibialis anterior muscles. However, a drawback of this approach is the requirement of ample space as the coils need to be positioned such that they encircle the nerve from four different sides.

Despite continuous efforts on both simulation and experimental fronts, there is still the need for performance improvement of magnetic stimulation before it can be regarded as a practical alternative approach to electric stimulation of PNS. Various coil designs have been examined to reduce the power requirement and generate more focused fields for selective activation of a particular neuronal population [21]–[33]. Figure-of-eight coils were first proposed by Maccabee *et al.* [21], and Hiwaki and Ueno [22] in the early 1990s. A figure-of-eight coil is constructed by wiring together two conventional cylindrical coils (as depicted in Fig. 1). Figure-of-eight coils are widely used for magnetic stimulation of CNS as the fields produced by these coils are stronger and more focused than that of conventional circular coils [34], [35]. Modifications of figure-of-eight coil designs, such as 4-leaf coil [23], three-dimensional differential coil [24], and bent figure-of-eight coils [32], have also been explored. Another coil design proposed for more focused field distribution is the slinky coil [25], built by adding a perpendicular coil at the joint of a figure-of-eight coil. Many modified versions of slinky coils have been designed [26], [27], including partial toroid shaped coils that also provided a more focused field and stimulation of deeper regions of the neural tissue [28], [29]. Other unconventional coil shapes, such as rectangular and U-shapes [30], have also been tested. However, a comprehensive study comparing 50 coil designs [31] (including those mentioned above) concluded that for all coil designs, improved field focality is achieved only at the expense of shallower electric field penetration. Further, none of the simulated coils displayed a depth-focality trade-off better than the figure-of-eight type coils [31]. Additionally, figure-of-eight coils require less volume compared to three-dimensional coil designs, such as slinky coils and differential coils.

Here, we optimize the figure-of-eight coil designs and investigate the effect of their orientation on the efficacy of peripheral nerve stimulation. As the orientations of figure-of-eight coils substantially affect the induced field distribution inside the nerve, stimulation using different orientations of figure-of-eight coil could provide selective stimulation. Coil orientations of figure-of-eight coil have been explored earlier for preferential activation of the cerebral cortex [36], [37], and

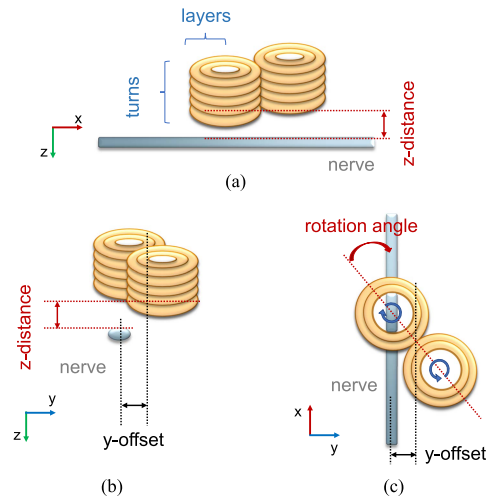


Fig. 1. Schematic of the simulation model with figure-of-eight coil and nerve: (a) nerve long-axis view (XZ-plane), (b) nerve cross-axis view (YZ-plane), and (c) top view (XY-plane). The coils in panels (a) and (b) have been drawn in a three-dimensional perspective to help with interpretation. The gap between the nerve and the coil, along  $z$ -axis, is defined as  $z$ -distance. The separation between the centers of nerve and figure-of-eight coil, along the  $y$ -axis, is represented by  $y$ -offset. The rotation angle represents the angle between a line passing through centers of two coils of figure-of-eight coil and  $x$ -axis. The direction of the current flow is illustrated in panel (c) by the blue arrows shown inside the inner diameter of each coil.

for increasing the size of motor evoked potentials from facial muscles such as Orbicularis Oris muscle [38] and Nasalis muscle [39]. Different coil orientations are also found to help modulate blood oxygenation changes during prefrontal TMS [40].

Although previous studies performed optimization of the figure-of-eight coil designs [41], [42] for neural stimulation, these studies considered much larger coils than those considered here. Further, in those studies, the authors ignored the effect of electric field distribution and compared coils in terms of the maximum induced electric field gradients. There are several works on the optimum positioning of circular and figure-of-eight coils with respect to the nerve for peripheral nerve stimulation [43]–[46]. However, these studies only focused on the translation of the coil and considered the figure-of-eight coil to be fixed at a perpendicular angle with respect to the nerve. Though Rouhonen *et al.* [47] and Sun *et al.* [48] experimentally analyzed figure-of-eight coils oriented parallel to the nerve as well, our work is more extensive as we have considered various intermediate orientation angles other than parallel and perpendicular cases. In summary, our work differs from above mentioned previous studies [41]–[49] in at least one of the following aspects. First, the coils used in previous studies are much larger (cm dimensions) than those we consider here (mm size). Second, the experimental works are focused on compound muscle action potentials (CMAPs), whereas we evaluate the minimum stimulation threshold required to elicit an action potential in the nerve fibers. Third, we provide a more comprehensive study on the effect of figure-of-eight coil design parameters and coil orientations, with respect to the nerve, in terms of stimulation threshold. Lastly, besides performing the coil optimization

analyses, we explore various coil orientation angles to study the scope of selectivity in peripheral nerve stimulation.

In this work, we optimize the design, orientation, and positioning of figure-of-eight coils for efficient and selective stimulation of the sciatic nerve, leveraging our previously developed simulation framework [50]. Simulations are performed using the multi-resolution impedance method and a  $\mu\text{m}$ -resolution heterogeneous multi-fascicular model of a rat sciatic nerve. The neural activation of nerve fibers is implemented in NEURON software [51] using an equivalent cable model with Frankenhaeuser-Huxley kinetics at the nodes of Ranvier and passive membrane properties for internodal myelin sheaths. First, we investigated how the figure-of-eight coil compares with a single cylindrical coil in terms of stimulation efficacy using a homogeneous tissue model. Next, we analyzed the effect of coil design parameters (such as the number of turns and number of layers of the coils) and coil configurations (same vs. opposite direction of coil currents, and series vs. parallel connection between two coils of a figure-of-eight coil) on the stimulation threshold. Then, we examined the change in the stimulation threshold for different orientations of the coil. Lastly, we computed the fields induced inside the heterogeneous nerve model due to various coil orientations and evaluated the extent of inter-fascicular selectivity.

## II. MODELS AND METHODS

### A. Overview of Simulation Model

A simple schematic of the simulation model is presented in Fig. 1. The nerve is positioned along the x-axis, and a figure-of-eight coil is placed over it. To be consistent with our earlier simulation and *in vivo* experimental results, we are assuming that the figure-of-eight coil is driven with a single set of stimulating hardware (e.g., Fig. 1 of [19]). Under this assumption, the figure-of-eight coil can be built by connecting two cylindrical coils either in series or parallel configuration. For both series and parallel configurations, current in the two coils of a figure-of-eight coil can be either in the same direction or opposite direction, depending upon how the two coils are attached. Therefore, there are four possible coil configurations based on how the two coils of a figure-of-eight coil are joined together:

- parallel connection, opposite current direction
- parallel connection, same current direction
- series connection, opposite current direction
- series connection, same current direction

For illustration, the figure-of-eight coil shown in Fig. 1 has two coils (each with 5 turns, 2 layers) with currents in the opposite direction (as shown in Fig. 1(c) using blue arrows inside the inner diameter of each coil). The minimum gap between the figure-of-eight coil and the nerve along the z-axis is defined as ‘z-distance’. The y-axis separation between the center of the figure-of-eight coil and the nerve center is called ‘y-offset’. The angle between the line passing through centers of two coils of the figure-of-eight coil and the x-axis is defined as ‘rotation angle’.

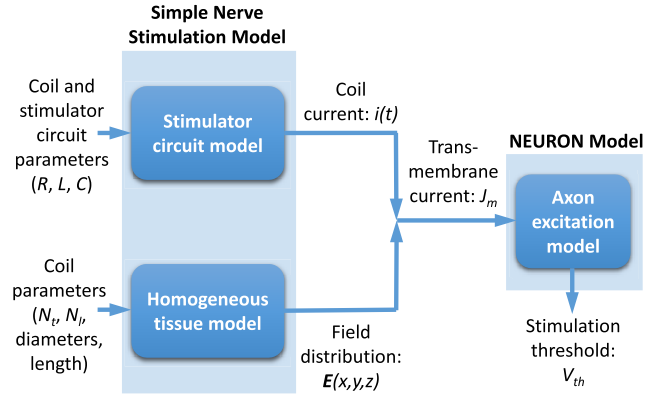


Fig. 2. Block diagram of simulation steps involved in parametric studies of stimulation threshold presented in Section III. The simulation framework utilizes a simple nerve stimulation model and axon excitation model to predict the stimulation threshold for considered coil design, positioning, and configuration. The simple nerve stimulation model consists of two components: 1) stimulator circuit model that provides the coil current waveform using electric parameters of the coil and stimulator circuit, and 2) homogeneous tissue model for computation of electric field distribution in the nerve, assuming a unit rate of change of coil current ( $\partial i / \partial t$ ). Electric field spatial distribution and coil current temporal waveform constitute the spatial-temporal transmembrane current ( $J_m$ ). The axon excitation model (implemented in NEURON) utilizes this  $J_m$  to predict the stimulation threshold required to evoke an action potential.

To compute induced fields and achieve neuronal activation by magnetic coils, we used our previously developed computational models and methods [50]. A heterogeneous multi-fascicular nerve model is constructed, and the multi-resolution impedance method is employed to evaluate the fields induced inside the modeled nerve. The computed field profiles are utilized to investigate activated neuronal populations and the possibility of stimulation selectivity. The multi-resolution impedance method helps in reducing the computational load and simulation duration. Nevertheless, given a large number of voxels, this model is computationally demanding for the substantial number of simulation runs required for parametric studies of coil optimization. Therefore, a simpler homogeneous tissue model is adopted to run simulations for comparative analyses. This faster approach is used to compute the change in the stimulation threshold due to changes in the coil design parameters, various coil orientations, and different coil-nerve distances. The modeling approach used for these parametric studies of stimulation threshold is summarized in Fig. 2, and results are presented in Section III. On the other hand, the comprehensive heterogeneous nerve model and multi-resolution impedance method are used for selectivity analyses presented in Section IV. The modeling approach utilized for selectivity analyses is outlined in Fig. 4. The details about all of these models and methods are presented below.

### B. Simple Nerve Stimulation Model for Parametric Studies

For parametric studies (presented in Section III), stimulation thresholds of various coil designs, configurations, positioning, and orientations are predicted using a simple nerve stimulation



model and an axon excitation model. The simulation steps and involved parameters are outlined in Fig. 2. The simple nerve stimulation model is based on previous studies [52], [53], and contains a homogeneous tissue model for faster field computations and a model for stimulator circuit representation. The homogeneous tissue model consists of a myelinated axon inside an infinite homogeneous medium (uniform conductivity) without including various tissue types and membranes present in the real nerve. The induced electric fields,  $\mathbf{E}(\mathbf{x}, \mathbf{y}, \mathbf{z})$ , inside the homogeneous tissue due to the considered stimulating coil are computed using analytical equation [54], [55], given below:

$$\mathbf{E}(\mathbf{r}, t) = -\frac{\mu}{4\pi} \frac{\partial i(t)}{\partial t} \int \frac{d\mathbf{l}}{|\mathbf{r} - \mathbf{r}'|} \quad (1)$$

where  $i(t)$  is the current flowing through the coil,  $\mathbf{r}$  is the position where the field is calculated,  $\mathbf{r}'$  is the position of a small segment of the coil, and  $d\mathbf{l}$  is the vector oriented along the direction of the coil segment. The electric field can be split into two components: 1) temporal variation, which is given by the rate of change of stimulation current,  $\partial i/\partial t$ , and 2) spatial distribution that is represented by the rest of the terms in Eqn. 1.

The neuronal activation of the myelinated axon is predicted using the axon excitation model (described in Section II-C). These predictions are made from the transmembrane current density,  $J_m$ , at the Nodes of Ranvier of the modeled axon, computed using the following equation [50]:

$$J_m = -0.00375 \left( \frac{\partial E_x}{\partial x} \right) d^2 \quad (2)$$

where  $J_m$  is transmembrane current density in mA/cm<sup>2</sup>,  $\partial E_x/\partial x$  is the gradient of the intracellular electric field along the nerve (with nerve positioned along the x-axis) in mV/mm<sup>2</sup>, and  $d$  is the axon diameter in  $\mu\text{m}$ . The spatial distribution of  $J_m$  is computed from the spatial component of the electric field in the homogeneous tissue model, whereas the temporal variation of  $J_m$  is estimated using the stimulator circuit model (as illustrated in Fig. 2). To decouple the spatial and temporal components of  $J_m$ , the electric field distribution is computed for unit rate of change of coil current,  $\partial i/\partial t$  (see Eqn. 1). In this way, the temporal variation of  $J_m$  is proportional to the rate of change of coil current. Thus, for every coil design, the current flowing through the coil,  $i(t)$ , is evaluated for the equivalent RLC circuit of the magnetic stimulator. Coil current, for the overdamped case, is given by the following equations:

$$i(t) = V_0 C \omega_2 (e^{-\omega_1 t}) \left( \left( \frac{\omega_1}{\omega_2} \right)^2 - 1 \right) \sinh(\omega_2 t) \quad (3)$$

where  $V_0$  is stimulator source voltage,  $C$  is stimulator discharge capacitance,  $\omega_1$  and  $\omega_2$  are given by:

$$\omega_1 = \frac{R}{2L}; \quad \omega_2 = \sqrt{\left( \frac{R}{2L} \right)^2 - \frac{1}{LC}} \quad (4)$$

Similarly, coil current for the underdamped case is computed using the following equations:

$$i(t) = V_0 C \omega_2 (e^{-\omega_1 t}) \left( \left( \frac{\omega_1}{\omega_2} \right)^2 + 1 \right) \sin(\omega_2 t) \quad (5)$$

where

$$\omega_1 = \frac{R}{2L}; \quad \omega_2 = \sqrt{\frac{1}{LC} - \left( \frac{R}{2L} \right)^2} \quad (6)$$

The stimulator discharge capacitor ( $C$ ) is 733  $\mu\text{F}$ , and the resistance ( $R$ ) and inductance ( $L$ ) of each coil design are evaluated, assuming that the coil is made up of 22 AWG wire with a wire diameter of 0.644 mm. Finally, the computed spatial-temporal transmembrane current density is sampled and applied at the nodes of Ranvier of the axon excitation model, and activation of the axon is predicted. Although fields and current densities computed using this model are relatively less accurate than those computed using the detailed heterogeneous nerve model [50], this homogeneous tissue model provides faster comparisons between coils with different configurations and design parameters. The mathematical equations to compute coil current waveform (using stimulator circuit model) and electric field distribution (using homogeneous tissue model) are implemented in MATLAB.

Our method to compute the induced electric field is similar to that used in the coil optimization study presented by Ruohonen *et al.* [42]. However, in their work, the authors have compared the coil designs only in terms of the maximum induced electric field gradient and ignored electric field distribution. Whereas, in our coil optimization analyses (Section III), we have also incorporated the effect of electric field distribution on the generation of an action potential, with the help of NEURON simulations (axon excitation model), as discussed in later paragraphs.

### C. Axon Excitation Model

For stimulation threshold predictions, a model of a myelinated axon is created in NEURON [51]. The axon diameter and g-ratio (ratio of axon diameter to axon diameter with myelin sheath) are 10  $\mu\text{m}$  and 0.625, respectively, based on the data presented in [56]. The total length of the modeled axon is 88 mm, with 55 Nodes of Ranvier separated by a distance of 1.6 mm. The axon is represented by an equivalent cable model with uniformly separated nodes of Ranvier and intermediate myelin sheaths, as in the myelinated nerve fiber model proposed by [57], [58]. Passive membrane properties represent the biophysics of myelin sheaths, and activation kinetics at the nodes of Ranvier are implemented using the Frankenhaeuser-Huxley (FH) equations [59]. The active ion channels include sodium current, potassium current, non-specific delayed current, and leak current. The membrane properties are tuned according to the experimental recordings of rat sciatic nerve [60]. A more accurate representation of myelinated axon can be achieved by double cable models [61], which can characterize the threshold fluctuations following an action potential. However, we aim to compare the stimulation threshold of various coil configurations and positioning, and the neuronal behavior in the recovery cycle is less important here. Further, it has been shown that despite being more complex, double cable models present similar sensitivity to pulse shape, amplitude, and axon diameter compared to single cable models [62]. Therefore, we considered a simple cable

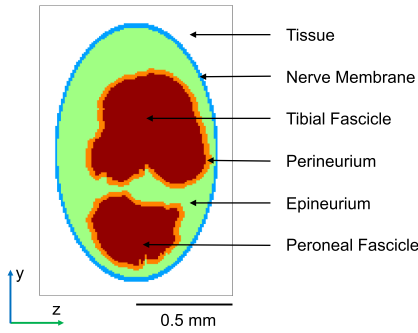


Fig. 3. Cross-sectional view of the sciatic nerve model. Different colors represent different tissue types: fascicles in red, perineurium in orange, epineurium (not including the outer layer) in green, nerve membrane (outer layer of the epineurium) in blue and connective tissue in white.

model with FH kinetics at the nodes of Ranvier to represent the axon.

As described in Section II-B and depicted in Fig. 2, for prediction of neuronal activation, spatial-temporal transmembrane current density ( $J_m$ ) computed at the Nodes of Ranvier is applied as an input to the axon excitation model (in a similar manner as in [54]). Initially, the stimulation circuit is assumed to have a 400 V DC voltage source. Next, to predict the stimulation threshold, this stimulation voltage value is increased or decreased (in increments of 4 V) to determine what voltage may elicit a spike event in the axon excitation model. The minimum value of the stimulator source voltage that is sufficient to evoke an action potential in the modeled axon is defined as the ‘stimulation threshold’. Further description of this axon excitation model is provided in [50].

#### D. Heterogeneous Nerve Model and Impedance Method for Selectivity Analyses

For stimulation selectivity analysis, we used a multi-fascicular heterogeneous three-dimensional model of the sciatic nerve, based on the histological image of the right sciatic nerve at the mid-thigh level of older rats from [56]. The modeled nerve has a length of 88 mm along the x-axis and has a maximum width of 1.66 mm and 0.88 mm along the y- and z-axes, respectively. Typically, the sciatic nerve of a rat has a roughly elliptical shape; to simplify the geometrical distribution of the tissue types, we have assumed the nerve’s outline to be elliptical. The cross-sectional view of the nerve model is shown in Fig. 3. The nerve contains two fascicles: tibial fascicle (upper fascicle in Fig. 3) and peroneal fascicle (lower fascicle in Fig. 3), with these two fascicles becoming the tibial and common peroneal nerves where the sciatic nerve bifurcates just proximal to the knee. The nerve model consists of various tissues present in the sciatic nerve, such as perineurium, epineurium, nerve membrane, and surrounding tissues. For an accurate representation of tissue heterogeneity, the spatial resolution of the model is 10  $\mu$ m along y- and z-axes. On the other hand, the resolution along the x-axis is 1 mm, which is on the order of the distance between two consecutive Nodes of Ranvier (assuming axon diameter of 10  $\mu$ m).

TABLE I  
CONDUCTIVITY OF VARIOUS TISSUE TYPES OF THE NERVE MODEL

Tissue Type	Conductivity ( $\sigma_x, \sigma_y, \sigma_z$ ) [S/m]
Fascicles	(0.33, 0.08, 0.08)
Perineurium	(0.01, 0.01, 0.01)
Epineurium	(0.1, 0.1, 0.1)
Nerve Membrane	(0.02, 0.02, 0.02)
Surrounding Tissue	(0.5, 0.5, 0.5)

TABLE II  
DETAILS OF MULTI-RESOLUTION SIMULATION STEPS

Steps	Resolution (x,y,z)	Number of voxels along (x,y,z) axes	Total number of voxels
step 1	1 mm, 0.25 mm, 0.25 mm	(91, 161, 81)	0.89 $\times 10^6$
step 2	1 mm, 0.05 mm, 0.05 mm	(91, 51, 31)	0.14 $\times 10^6$
step 3	1 mm, 0.01 mm, 0.01 mm	(89, 181, 101)	1.66 $\times 10^6$

For the impedance method implementation, the simulation domain is discretized into cuboidal voxels. Various tissue types of the model are represented by corresponding impedance values at each side of the voxel. The impedance values at the sides of the voxel depend on the voxel size and conductivity properties of the tissue types [63]. The impedance values are calculated using the following equation:

$$Z(\mathbf{r}) = \frac{L_v}{(\sigma(\mathbf{r}) + j2\pi f \epsilon_r \epsilon_0) A_v} \quad (7)$$

where  $Z(\mathbf{r})$  is the impedance at the side of the voxel,  $\sigma(\mathbf{r})$  is the conductivity of the tissue type (see Table I),  $A_v$  is the cross-sectional area of the voxel,  $L_v$  is the length of the voxel side,  $f$  is the operating frequency,  $\epsilon_0$  is the absolute permittivity, and  $\epsilon_r$  is the relative permittivity of the medium. The conductivity values of these tissue types are based on the literature [64] and are presented in Table I. Given the low operating frequencies of the stimulator, the imaginary part of the impedance is negligible compared to the real part; therefore, we assumed only real impedance values in this work.

For field computations, first, the magnetic field at each voxel of the simulation model is computed using Biot–Savart law for the given coil design and orientation. The computed magnetic field and impedance values are then used to compute the induced electric field with the help of Faraday’s law of induction, implemented in the impedance method. The simulation steps are outlined in the block diagram of Fig. 4. The multi-resolution approach is leveraged to minimize the number of voxels in the simulation domain, which helps reduce the computational load and time. Each simulation is performed in three steps. In the first step, the entire simulation space is considered with a coarse spatial resolution of 0.25 mm (along y- and z-axes). Gradually, in the following steps, a finer spatial resolution is used, and simulation space is truncated by trimming the layers of voxels near the boundaries. The model size, resolution, and number of voxels used in each simulation step are provided in Table II. The boundary conditions at each step are computed from the previous step to maintain the accuracy of the computed fields. The superposition principle is used to compute the fields due to the two coils of the

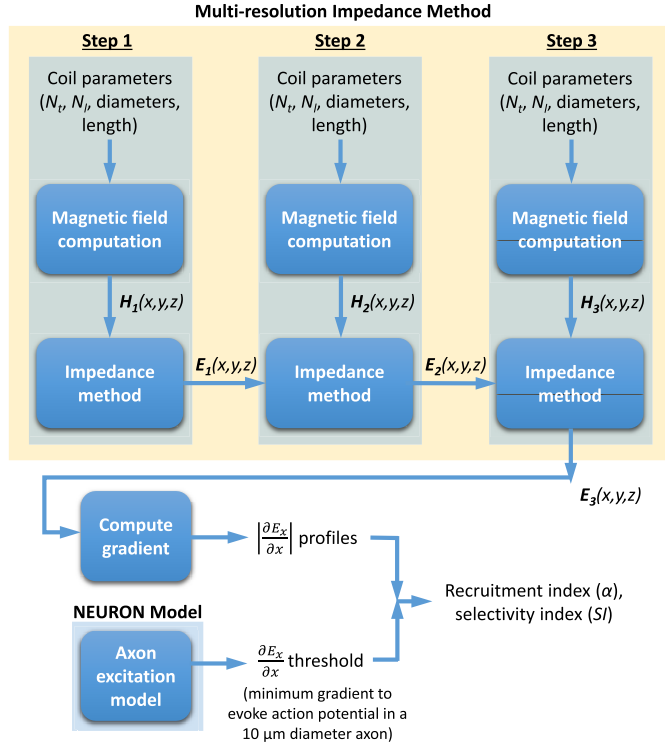


Fig. 4. Block diagram of simulation steps involved in selectivity analyses presented in Section IV. The field computations are performed using the multi-resolution impedance method in three steps. The model size is progressively reduced, and spatial resolution is further refined from step 1 to step 3, as indicated in Table II. At each step, first, the magnetic field due to the coil is computed, and then the electric field induced inside the modeled nerve is computed using the impedance method. Electric field values obtained at a simulation step are used to find the boundary conditions of the next step. The final (step 3) electric field values are used to compute the electric field gradient profiles inside the modeled heterogeneous nerve. Finally, recruitment and selectivity indices of nerve fascicles are estimated with respect to the  $\partial E_x/\partial x$  threshold for a 10  $\mu\text{m}$  diameter axon.

figure-of-eight coil. The Biot–Savart law (for the computation of magnetic fields) and the impedance method are implemented using FORTRAN programming language. Further details about field computations using the impedance method are documented in [20], [50].

As shown in Fig. 4, the electric fields computed at step 3 of the multi-resolution impedance method are used to estimate the field gradients and recruitment of various regions of the nerve. The activation of an axon is mainly dependent on the spatial distribution of the electric field gradient along the nerve ( $\partial E_x/\partial x$ ). Therefore, after completing step 3 of the simulations, we computed the field gradient,  $\partial E_x/\partial x$ , inside the modeled heterogeneous nerve by performing numerical differentiation for each voxel of the simulation model. Unlike the simple nerve stimulation model (see Fig. 2), impedance method simulations are not directly coupled with the axon excitation model (implemented in NEURON). To evaluate the recruitment of various regions of the nerve, we compared the field gradient at each voxel of the model with a  $\partial E_x/\partial x$  threshold. The ‘ $\partial E_x/\partial x$  threshold’ is the minimum  $\partial E_x/\partial x$  value that could evoke an action potential in the axon of a given diameter. Here, we considered the  $\partial E_x/\partial x$  threshold value of 5 mV/mm<sup>2</sup>, which is found with the help of the

axon excitation model, considering a 10  $\mu\text{m}$  diameter myelinated axon. Thus, we assumed that the action potential is evoked in the axon if the gradient along the axon at any location is greater than or equal to the  $\partial E_x/\partial x$  threshold value of 5 mV/mm<sup>2</sup>.

We analyzed field gradient profiles of all considered coil orientations (*rotation angles*) and translations (*y-offsets*) to assess the possibility of selective stimulation. To quantify the stimulation selectivity of a particular region (including only fascicles, not the entire nerve), we defined two assessment parameters: recruitment index ( $\alpha$ ) and selectivity index ( $SI$ ) as in [20]. The recruitment index of a region is computed by estimating the proportion of the voxels that exceed the  $\partial E_x/\partial x$  threshold. The definition of recruitment index of the  $i^{\text{th}}$  region,  $\alpha_i$ , is given by:

$$\alpha_i = \frac{A_i}{A_T} \quad (8)$$

where  $A_i$  is the stimulated area in the region (i.e., area that surpasses the  $\partial E_x/\partial x$  threshold), and  $A_T$  is the total area of the target region. The selectivity index is based on the recruitment of various considered regions. The selectivity index of the  $i^{\text{th}}$  region is computed using the following equation:

$$SI_i = \alpha_i - \frac{1}{n-1} \sum_{j=1, j \neq i}^n \alpha_j \quad (9)$$

where  $\alpha_i$  is the recruitment index of the  $i^{\text{th}}$  region, and  $n$  is the number of different regions of the nerve considered. The selectivity index varies from  $-1$  (zero recruitment of targeted region and complete recruitment of the rest of the regions) to 1 (complete recruitment of the targeted region without any recruitment of the rest of the regions). Computation of the field gradients and estimation of the recruitment and selectivity indices are performed using MATLAB scripts.

We have extensively validated these simulation models and methods in our previous work [50], [65], [66]. We computed the stimulation thresholds using both homogeneous and heterogeneous nerve models and compared those with the *in vivo* experimental results [50]. Coils with different design parameters were used to confirm that the models represent the experimental conditions correctly, and the simulation frameworks accurately predict the stimulation thresholds. As presented in [50], for all coil designs, the predicted stimulation thresholds were found to be in good agreement with the *in vivo* experimental results. Although the threshold values predicted by the heterogeneous nerve model were found to be more accurate, the values predicted using the homogeneous model were close to the experimental results as well.

### III. STIMULATION THRESHOLD ANALYSES: PARAMETRIC STUDIES

#### A. Coil Configurations

In the first set of simulations, we compared all four electrical configurations (parallel vs. series connection, opposite vs. same current direction) of a figure-of-eight coil with a

TABLE III  
LIST OF FIXED PARAMETERS VALUES AND VARYING PARAMETERS RANGES USED IN THE SIMULATIONS

Fig. No.	Configuration	$N_t$	$N_l$	$z$ -distance (mm)	rotation angle	$y$ -offset (mm)
Fig. 5	parallel-opposite, parallel-same, series-opposite, series-same	5	7	0.5 to 2.5, interval 0.5	90°	aligned with $ \partial E_x / \partial x _{max}$
Fig. 6	parallel-opposite	2 to 10	4 to 12	0.5	90°	aligned with $ \partial E_x / \partial x _{max}$
Fig. 7	parallel-opposite, parallel-same	5	7	0.5	0° to 90°, interval 10°	aligned with $ \partial E_x / \partial x _{max}$
Fig. 9, 10, 11	parallel-opposite	5	7	0.5	0° to 90°, interval 30°	-6 to 6, interval 1

single cylindrical coil by examining the stimulation threshold as a function of coil-nerve separation ( $z$ -distance). The considered cylindrical coil has 5 turns and 7 layers. Similarly, both coils of the figure-of-eight coil have 5 turns and 7 layers. This choice for the number of turns and layers is based on the parametric study presented in Section III-B. The figure-of-eight coils are oriented with respect to the nerve by a 90° rotation angle as it leads to a minimum stimulation threshold for all coil configurations (discussed in Section III-C). In the case of a single solenoidal coil, it has been shown that the induced field inside the nerve is maximum when the coil is placed at an offset from the nerve [67]. Further, the stimulation threshold is found to be minimum when the nerve passes through the maxima of the electric field gradient magnitude,  $|\partial E_x / \partial x|$ . Therefore, for every coil configuration and  $z$ -distance, we selected the  $y$ -offset value that aligns the nerve with the maxima of  $|\partial E_x / \partial x|$ .

Using the simple nerve stimulation model and axon excitation model, we predicted the stimulation thresholds for neuronal activation. The predicted stimulation thresholds of the considered cylindrical coil and all four figure-of-eight coil configurations are presented in Fig. 5. As expected, the stimulation threshold for each case increases with  $z$ -distance between the nerve and the coil. A figure-of-eight coil with a series connection requires a higher stimulation threshold than the coil with a parallel connection. The reason for this threshold increase is the higher resistance and inductance of the figure-of-eight coil in the case of series connections in comparison to parallel connections. When comparing series and parallel connection, assuming the same coil current, the spatial distribution of the electric field inside the tissue remains the same. However, the higher resistance and inductance of the coil with a series connection leads to a coil current waveform with a lower rate of change,  $\partial i / \partial t$ . Therefore, coils with the series connection require more stimulator source voltage to generate sufficient transmembrane current for evoking an action potential inside the nerve fiber.

The opposite direction of current flow in two coils of the figure-of-eight coils leads to lower stimulation thresholds than the same direction of current flow. As long as the coil connection type (series or parallel) is unchanged, electric properties of the figure-of-eight coil ( $R$ ,  $L$ ), with both the same and opposite direction of current flow, remain the same. Despite having the same current waveform (and same  $\partial i / \partial t$ ), the configuration with the opposite direction of current flow

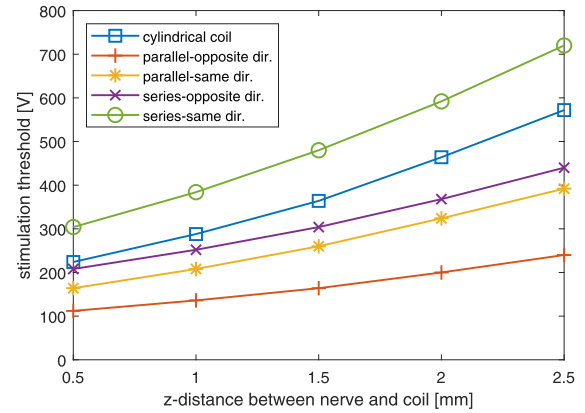


Fig. 5. Comparison of stimulation threshold with respect to  $z$ -distance for cylindrical coil and various electrical configurations of the figure-of-eight coil. The figure-of-eight coils are oriented by 90° rotation angle, and the  $y$ -offset is selected such that it leads to the minimum threshold for the considered case.

generates focused fields at the center of the figure-of-eight coil. Consequently, this configuration generates higher induced fields at the stimulation site and results in a relatively lower stimulation threshold than coil configurations with the same current direction. It can be observed in Fig. 5 that figure-of-eight coils with the series coil connection and the same current direction result in the highest stimulation threshold, followed by the cylindrical coil. On the other hand, figure-of-eight coils with parallel coil connection and the opposite current direction lead to the lowest stimulation threshold. For the  $z$ -distance of 0.5 mm, this figure-of-eight configuration requires a 50% lower threshold compared to the cylindrical coil. From here onwards, the  $z$ -distance between the coil and the nerve is set at 0.5 mm, which is on the order of magnitude comparable to those utilized in our *in vivo* experiments [19], [50], [65]. Table III provides the list of fixed parameters (with considered values) and varied parameters (with considered ranges) used in various analyses and results of this paper.

### B. Effect of Number of Layers and Turns

To analyze the effect that the number of layers ( $N_l$ ) and turns ( $N_t$ ) of the coil on the stimulation threshold, we considered figure-of-eight coils with various values of  $N_l$  and  $N_t$ . The layers and turns of a coil are defined as in Fig. 1. Every figure-of-eight coil is made by combining two cylindrical coils, both with a fixed inner diameter of 2.0 mm. In order to limit



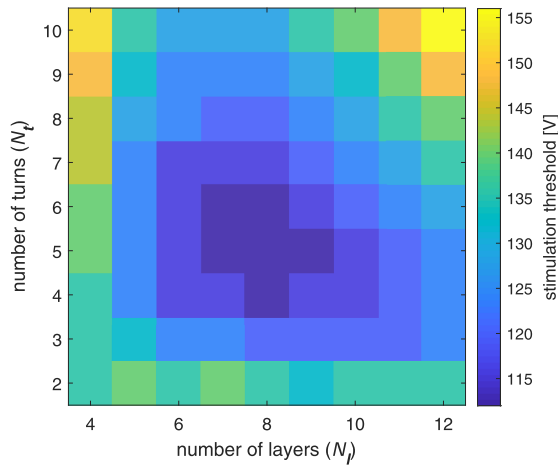


**Fig. 6.** Stimulation threshold for figure-of-eight coils with respect to the number of turns and layers. The coils are considered to have an electrical configuration involving a parallel coil connection and opposite current direction. The *rotation angle* and *z-distance* are assumed to be  $90^\circ$  and  $0.5$  mm, respectively. The *y-offset* is selected such that it results in the minimum threshold for the considered case.

the number of cases for simulations, both coils of the figure-of-eight coil are considered to have the same  $N_l$  and  $N_t$  values. Thus, a higher value of  $N_l$  represents a coil with a broader cross-section, and a higher value of  $N_t$  indicates a taller coil. In this study, the parameters  $N_l$  and  $N_t$  take integer values from 4 to 12 and from 2 to 10, respectively. These ranges result in the outer diameters between  $7.2$  mm and  $17.7$  mm, and lengths between  $1.3$  mm and  $6.5$  mm. For this study, only coil electrical configuration with the lowest stimulation threshold (i.e., parallel connection and opposite current directions) is considered.

The two-dimensional grid plot of predicted stimulation thresholds for the considered ranges of  $N_l$  and  $N_t$  is presented in Fig. 6. The three-dimensional stimulation threshold plot forms the shape of a bowl with high values near the edges and lower values around  $N_t = 5$  and  $N_l = 8$ . For fixed  $N_l$  and increasing  $N_t$ , the predicted stimulation threshold first decreases and then starts increasing. Similarly, the stimulation threshold for the coils with a fixed  $N_t$  first shows reduction and then grows with an increase in  $N_l$ . We found that increasing the number of turns (or layers) reduces the rate of change of coil current  $\partial i / \partial t$  (due to higher coil resistance and inductance) and increases the magnitude of the induced electric field gradient (per unit  $\partial i / \partial t$ ). As the number of turns (or layers) increases, even though  $\partial i / \partial t$  reduces, an increase in induced field gradients (per unit  $\partial i / \partial t$ ) dominates and leads to the reduction of the stimulation threshold. However, after a certain value of  $N_t$  (or  $N_l$ ), even though electric field gradients (per unit  $\partial i / \partial t$ ) continue to increase,  $\partial i / \partial t$  starts reducing more rapidly, resulting in an increase in the stimulation threshold. In other words, for very small  $N_t$  (or  $N_l$ ), even though coil current is large, the electric field gradient (per unit  $\partial i / \partial t$ ) is much weaker, and therefore, the stimulation threshold is high. Conversely, for very large  $N_t$  (or  $N_l$ ), though the electric field (per unit  $\partial i / \partial t$ ) is larger, the coil current is much smaller, and again stimulation threshold is high. This implies that the optimum value of  $N_t$  (or  $N_l$ ) for the lowest stimulation

threshold falls between these two extreme cases. This trade-off between coil currents and induced field gradients results in the bowl-like shape (smaller values around the center and higher values around the boundaries of the grid plot in Fig. 6) of predicted stimulation thresholds. Note that, though the reasoning mentioned above is entirely based on the magnitudes of  $\partial i / \partial t$  and electric field gradients, the stimulation thresholds presented in Fig. 6 are computed using the simulations that incorporate the impact of temporal variation of coil current and the spatial distribution of electric fields as well.

As displayed in Fig. 6, the lowest (and identical) stimulation threshold of  $112$  V is found for six coil designs (number of turns and layers in the  $\{N_t, N_l\}$  format):  $\{4, 8\}$ ,  $\{5, 7\}$ ,  $\{5, 8\}$ ,  $\{5, 9\}$ ,  $\{6, 7\}$  and  $\{6, 8\}$ . We selected the coil with 5 turns and 7 layers for the rest of the simulations, as it has the smallest volume and the least number of layers among these six coils. A lesser number of layers means a smaller cross-sectional area of the coil, which leads to a narrower hot spot of the fields. Therefore, the coil with 5 turns and 7 layers may provide better selectivity compared to wider coils. Both coils of this figure-of-eight coil have an outer diameter of  $11.1$  mm and a length of  $3.3$  mm (and an inner diameter of  $2.0$  mm). For parallel configuration of this figure-of-eight coil, resistance ( $R$ ) and inductance ( $L$ ) are  $19.1$  m $\Omega$  and  $2.2$   $\mu$ H, respectively; whereas, for series configuration,  $R$  is  $76.6$  m $\Omega$ , and  $L$  is  $8.9$   $\mu$ H. Note that the mutual inductance between the two coils of the figure-of-eight coil is ignored, allowing superposition in the simulation. The response of the stimulator circuit is underdamped in the cases of both parallel and series configuration of this figure-of-eight coil. For parallel configuration, the damping factor and damped frequency are  $0.73$  and  $16.8$  kHz, respectively; whereas, for series configuration, the damping factor is  $0.63$  and the damped frequency is  $9.6$  kHz.

### C. Coil Orientations

Next, different orientations of the figure-of-eight coil with respect to the nerve are explored. The *rotation angle* is varied from  $0^\circ$  to  $90^\circ$  with increments of  $10^\circ$ , and the stimulation threshold is predicted for each *rotation angle*. The *y-offset* is selected such that the nerve passes through the maxima of  $|\partial E_x / \partial x|$ . The predicted stimulation threshold and optimal *y-offset* values for two coil configurations (parallel coil connection and same vs. opposite current direction) are presented in Fig. 7(a) and in Fig. 7(b), respectively. The other two configurations of figure-of-eight coil (series coil connection and same vs. opposite current direction) require a higher threshold than their parallel connection counterparts (data not shown). However, for both series and parallel connection cases, the change in threshold with respect to *rotation angle* follows a similar trend. For clarity, the data points in Fig. 7(b) are shifted slightly left (for opposite direction configuration) and right (for the same direction configuration) of the actual angle simulated.

For coil configuration with the opposite current direction, the stimulation threshold only slightly varies as the *rotation angle* increases from  $0^\circ$  to  $40^\circ$ . Whereas the stimulation



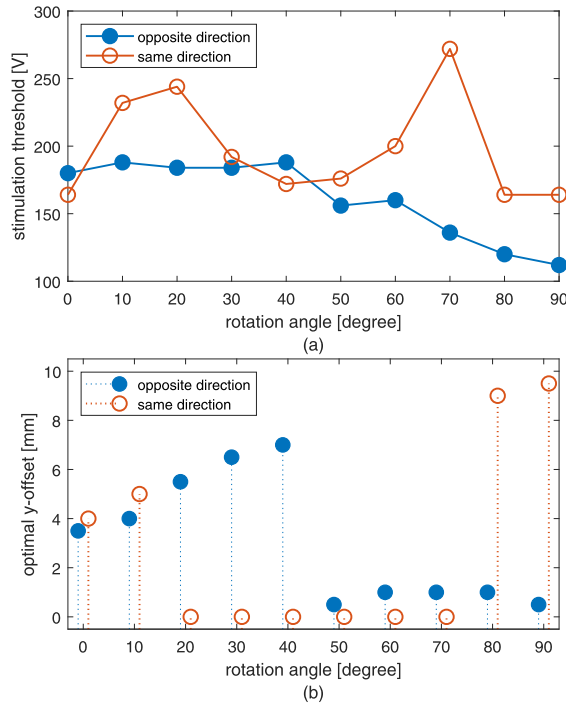


**Fig. 7.** Effect of coil orientations on stimulation threshold: (a) stimulation threshold with respect to the *rotation angle*, (b) optimal *y-offset* that results in minimum stimulation threshold for the given case. For clarity, the data points in panel (b) are shifted slightly left or right of the actual angle simulated. Coil configurations with parallel connection and same vs. opposite current direction are plotted. Red unfilled circles represent figure-of-eight coils with the same direction of current in its two coils; whereas, blue filled circles represent coils with the opposite current direction. The *z-distance* is 0.5 mm, and the *y-offset* is selected such that the nerve passes through the maxima of  $|\partial E_x / \partial x|$ .

threshold generally decreases as the *rotation angle* increases from 40° to 90°. We observed that for the smaller angles, the gradient of the electric field along the nerve,  $\partial E_x / \partial x$ , is lower. For angles greater than 40°,  $\partial E_x / \partial x$  increases as the *rotation angle* approach 90°. The lowest stimulation threshold of 112 V is observed for 90° *rotation angle*. The optimal *y-offset* for opposite current directions increases as the rotation angle is changed from 0° to 40° (Fig. 7(b)). The smaller angles require non-zero *y-offset* values as the field gradient is not focused at the center of coils for these cases. Whereas for angles greater than 40°, the optimal *y-offset* is almost zero, i.e., the minimum stimulation threshold is observed when the figure-of-eight coil center nearly aligns with the nerve axis.

For coil configuration with the same current direction, the stimulation threshold is predicted to be lowest and identical (164 V) for 0° and 90° *rotation angles*. For most of the coil orientations, the stimulation threshold for the same direction of current flow is larger or nearly equal to that of the opposite direction. Unlike that observed for the opposite direction, the optimal *y-offset* for the same direction of current flow has two discontinuities. The optimal *y-offset* values are found to be zero for angles from 20° to 70°. For angles 80° and 90°, the optimal *y-offset* is 9 mm and 9.5 mm, respectively, which is close to the diameter of each coil of the figure-of-eight coil. We found that the *y-offset* value changes the stimulation threshold drastically. Therefore, to minimize the stimulation

threshold, the coil position with respect to the nerve needs to be optimized.

#### IV. STIMULATION SELECTIVITY ANALYSES

Next, we investigated whether these coil orientations could exhibit selective stimulation. As the series connection coil configurations lead to higher stimulation thresholds, we only considered two figure-of-eight configurations: 1) parallel coil connection with the opposite current direction and 2) parallel coil connection with the same current direction. For the results presented here onwards, we performed the simulations using the heterogeneous multi-fascicular nerve model (described in Section II-D). In order to limit the number of simulations, we considered four *rotation angles*: 0°, 30°, 60°, and 90°. The range of *y-offset* values is from -6 mm to 6 mm with an increment of 1 mm, leading to 104 simulation sets. As the impedance method is a frequency-domain solver, simulations need to be performed at multiple frequencies to consider specific coil current waveforms. Given the larger number of simulation sets, considering multiple frequencies require a very long simulation time. Therefore, we assumed that the coils are driven by a sinusoidal current with a peak of 30 A and a frequency of 16.8 kHz (which is also the damped frequency for the considered coil configurations).

As described in Section II-D, these simulations are performed in three steps, with each succeeding step simulating a smaller region with finer resolution (see Table II). The XY-slices of electric field component,  $E_x$ , of the first step of the simulation (using coil configuration with the opposite current direction) are presented in Fig. 8. Each field profile of Fig. 8 presents the XY-slice at  $z = -0.5$  mm ( $z = 0$  mm represents the nerve center). The field profile for 0° *rotation angle* appears similar to that of two single cylindrical coil placed side by side (data not shown). As the angles increase from 0° to 90°, the coupling between the fields of both coils of the figure-of-eight coil starts to intensify.

We analyzed the inter-fascicular selectivity attained using all 104 simulation sets of considered coil configurations, orientations, and translations. These simulation sets are compared in terms of the corresponding electric field profiles and resulting recruitment indices and selectivity indices (as described in Section II-D). Among these 104 cases, we selected the ones with relatively higher selectivity indices and paired them in groups of two such that one case leads to the selectivity of the tibial fascicle, and the other case results in selectively activating the peroneal fascicle. In order to switch between activation of two fascicles without much alterations in coil configuration, orientation, and translation, we chose the pairs such that the two cases of each pair differ only in one variable (either coil configuration or orientation or translation). Three examples of these pairs, along with the target fascicle for each case, are presented in Table IV. In the first pair, only directions of coil currents are switched, while *rotation angle* and *y-offset* are the same for both cases. Similarly, in the second pair, only *rotation angles* are different, whereas coil configuration and translation are identical. Lastly, in the third pair, coil configuration and orientation are the same, and only *y-offsets* are unlike. The last two columns of Table IV present the

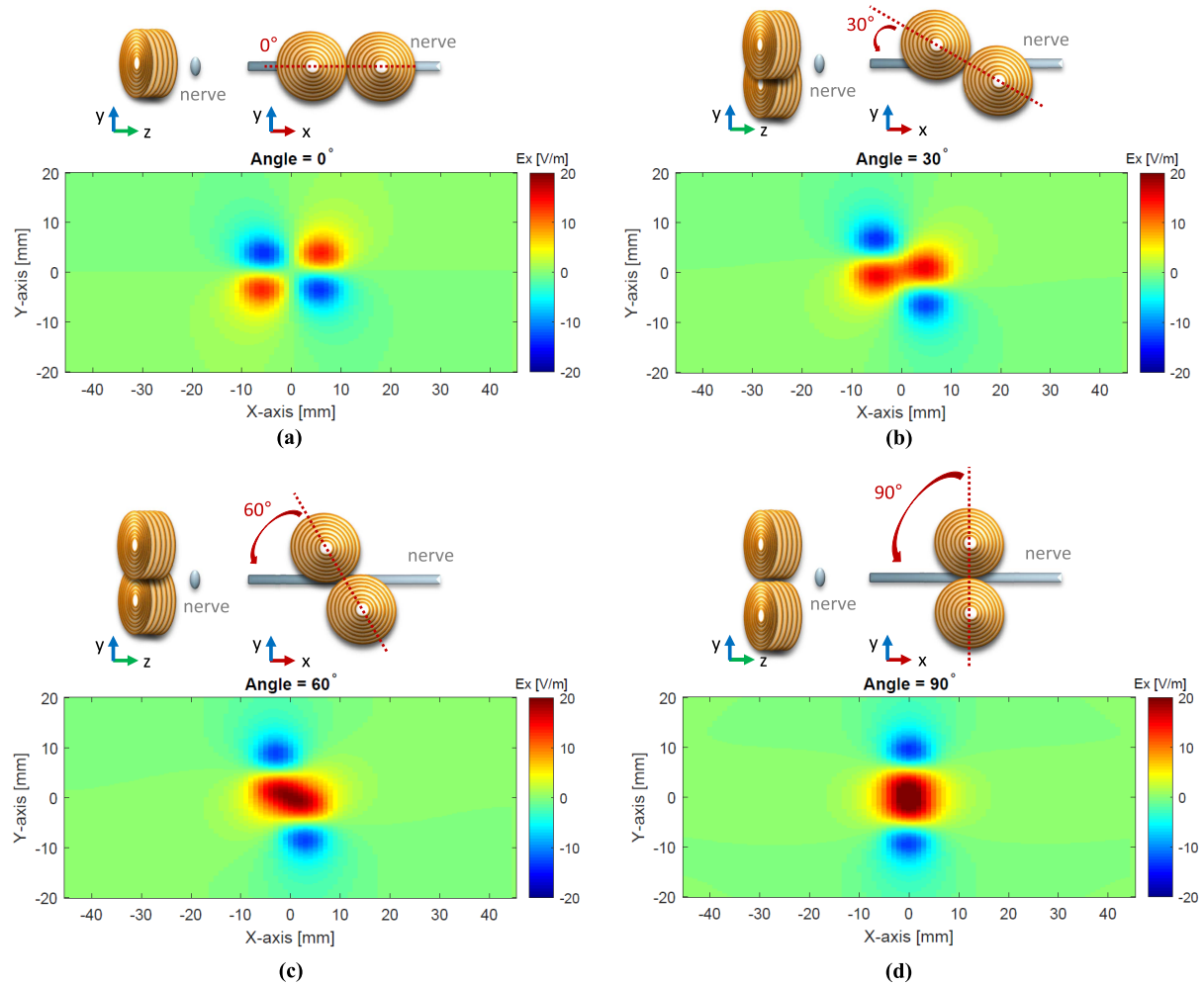


**Fig. 8.** Electric field profiles for 0°, 30°, 60°, and 90° rotation angles. The rotation angles are mentioned on top of each field profile. Each field profile presents the XY-slices of electric field component,  $E_x$ , at  $z = -0.5$  mm. The coils have an electrical configuration with parallel coil connection and opposite current direction, and the  $y$ -offset is 0 mm for all profiles. A sinusoidal current drives the coils with a peak of 30 A and a frequency of 16.8 kHz. The corresponding YZ-plane and XY-plane views of the coil and nerve are illustrated on the left of each field profile.

**TABLE IV**  
CASES FOR INTER-FASCICULAR SELECTIVITY

Pairs	Target fascicle	rotation angle	$y$ -offset	Current direction	$SI$	$SI_{10}$
pair 1	tibial	90°	6 mm	opposite	0.85	0.76
	peroneal	90°	6 mm	same	0.80	0.71
pair 2	tibial	60°	-6 mm	same	0.95	0.71
	peroneal	0°	-6 mm	same	1.00	0.81
pair 3	tibial	60°	4 mm	opposite	0.99	0.86
	peroneal	60°	-4 mm	opposite	0.93	0.86

selectivity indices ( $SI$ ) for  $\partial E_x / \partial x$  threshold of 5 mV/mm<sup>2</sup> and the minimum selectivity indices for  $\partial E_x / \partial x$  thresholds within  $\pm 10\%$  variations (i.e., for  $\partial E_x / \partial x$  threshold values between 4.5 to 5.5 mV/mm<sup>2</sup>), denoted by  $SI_{10}$ .

Among the case pairs that differ only in coil configurations, maximum inter-fascicular selectivity is achieved for the orientation angle of 90° and  $y$ -offset of 6 mm (pair 1 in Table IV). The field gradients of the electric field profiles for these cases are shown in Fig. 9(a) and 9(c). The gradient distribution changes its focus from tibial fascicle to peroneal fascicle as

the coil currents in the figure-of-eight coil change from the opposite direction to the same direction. We scaled the coil currents to incorporate the activation of most of the axons of a fascicle while simultaneously minimizing activation in the other fascicle. For the upper panels of Fig. 9, coil currents are in the opposite direction with a current peak of 270 A, whereas for the lower panels, coil currents are in the same direction with a peak of 320 A. Fig. 9(b) and 9(d) present the recruitment indices of tibial and peroneal fascicles with respect to  $\partial E_x / \partial x$  threshold using solid blue and dashed blue curves, respectively. The selectivity indices of tibial and peroneal fascicles are shown using red dotted curves in Fig. 9(b) and 9(d), respectively. We attained a maximum selectivity index of 0.85 for the tibial fascicle and 0.80 for the peroneal fascicle, considering the  $\partial E_x / \partial x$  threshold of 5 mV/mm<sup>2</sup> (vertical dashed black line in Fig. 9(b) and 9(d)). These results suggest that a properly oriented and translated figure-of-eight coil could provide selective activation of one fascicle over another, simply by scaling and switching currents between opposite and same directions within the two coils of the figure-of-eight coil. Even for  $\pm 10\%$  variations in the

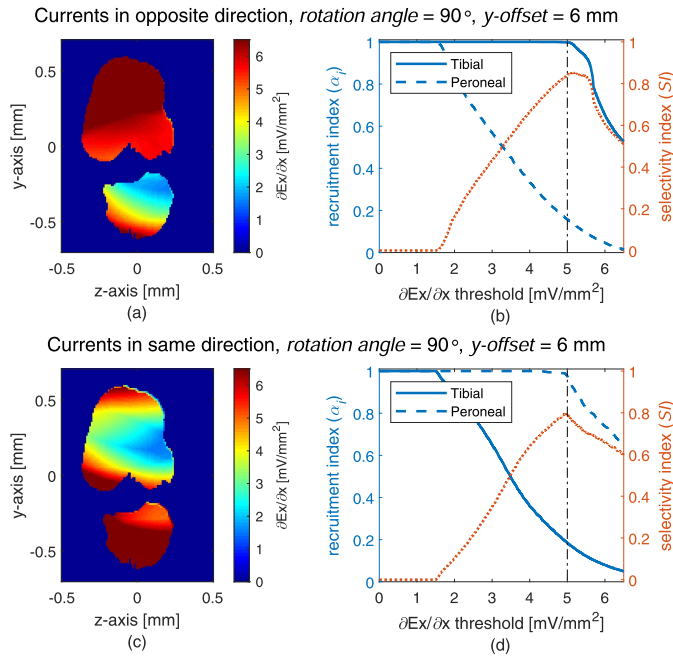
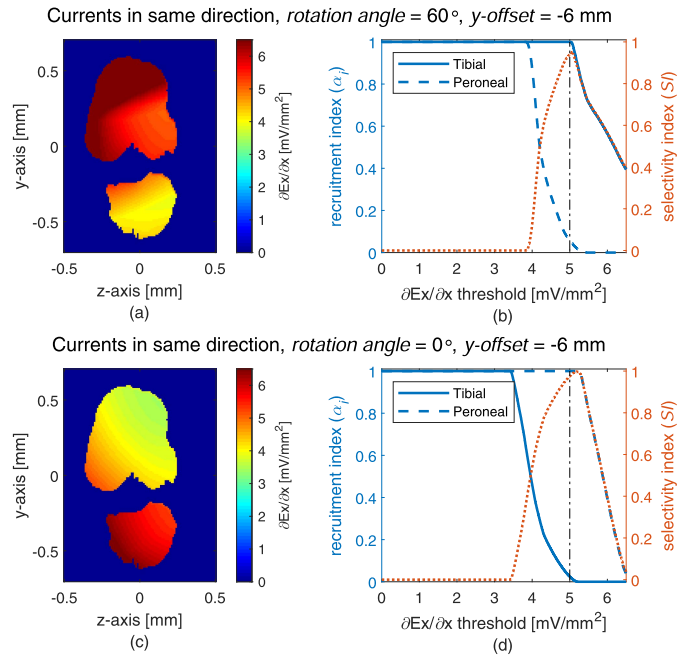


**Fig. 9.** Inter-fascicular selectivity achieved by figure-of-eight coil configurations with coil currents in opposite vs. same directions. Both cases have coils positioned with  $90^\circ$  rotation angle and 6 mm  $y$ -offset. Panels (a) and (b) show electric field gradients and recruitment indices, respectively, for coil configuration with currents in the opposite direction with a peak of 270 A. Similarly, panel (c) displays electric field gradients, and panel (d) shows recruitment indices for a coil configuration with currents in the same direction with a peak of 320 A. The selectivity indices for tibial and peroneal fascicles are plotted in red in (b) and (d), respectively. The  $\partial E_x/\partial x$  threshold of  $5 \text{ mV/mm}^2$  is highlighted by a black dashed vertical line.

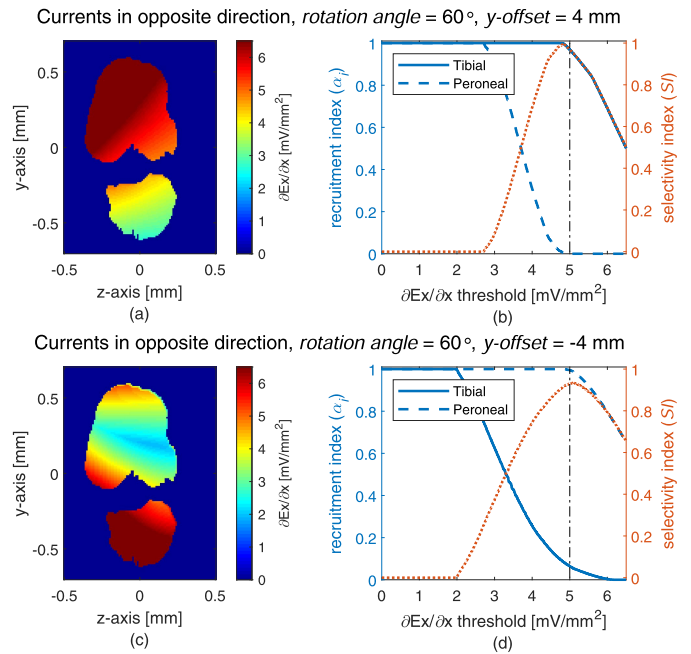
considered  $\partial E_x/\partial x$  threshold, the minimum selectivity indices ( $SI_{10}$ ) for tibial and peroneal fascicles are 0.76 and 0.71, respectively.

Fig. 10 and Fig. 11 present electric field gradients, recruitment and selectivity indices for pair 2 and pair 3 of Table IV, respectively. In Fig. 10, the coil configurations (with the same current directions) and  $y$ -offset (of -6 mm) are consistent for both cases, whereas rotation angles are  $60^\circ$  and  $0^\circ$  for upper and lower panels, respectively. We can observe from Fig. 10(a) and Fig. 10(b) that switching rotation angle from  $60^\circ$  to  $0^\circ$  leads to a change in the focus of field gradient distribution from tibial to peroneal fascicle. For the  $\partial E_x/\partial x$  threshold of  $5 \text{ mV/mm}^2$ , selectivity indices of 0.95 and 1.00 are found for tibial fascicle and peroneal fascicles, respectively. For upper panels of Fig. 10, coil currents have a peak of 160 A, and for lower panels, the coil current peak is 100 A.

In Fig. 11, the coil configurations (with the opposite current directions) and rotation angles (of  $60^\circ$ ) are identical for both cases, whereas  $y$ -offsets are 4 mm and -4 mm for upper and lower panels, respectively. Changing the  $y$ -offset from 4 mm to -4 mm steers the focus of field gradient distribution from tibial to peroneal fascicle. Considering the  $\partial E_x/\partial x$  threshold of  $5 \text{ mV/mm}^2$ , we found the selectivity indices of 0.99 and 0.93 for tibial and peroneal fascicles, respectively. Coil current peaks are 130 A and 170 A for the upper and lower panels of Fig. 11, respectively. Though the selectivity indices ( $SI$  and  $SI_{10}$ ) are slightly lower for the cases of Fig. 9



**Fig. 10.** Inter-fascicular selectivity achieved by figure-of-eight coil orientations with  $60^\circ$  vs.  $0^\circ$  rotation angles. Both cases comprise of  $y$ -offsets of -6 mm and coil configurations with coil currents in the same directions. Panels (a) and (b) show electric field gradients and recruitment indices, respectively, for rotation angle of  $60^\circ$ . Similarly, panel (c) and (d) present electric field gradients and recruitment indices for rotation angle of  $0^\circ$ .



**Fig. 11.** Inter-fascicular selectivity achieved by figure-of-eight coil translations with 4 mm vs. -4 mm  $y$ -offset. Both cases comprise of rotation angles of  $60^\circ$  and coil configurations with coil currents in the opposite directions. Panels (a) and (b) show electric field gradients and recruitment indices, respectively, for  $y$ -offset of 4 mm. Similarly, panel (c) and (d) display electric field gradients and recruitment indices for  $y$ -offset of -4 mm.

(pair 1 of Table IV) than those of Fig. 10 and 11 (pair 2 and pair 3 of Table IV), it is practically easier to simply change the directions of the coil currents instead of changing the

orientation or positioning of the coil in order to switch between activation of tibial and peroneal fascicles.

These findings suggest that inter-fascicular selectivity (with  $SI \geq 0.80$ ) can be obtained by changing only *rotation angle*, *y-offset*, or coil current direction and accordingly scaling the currents in the two coils of the figure-of-eight coil. For all the discussed cases, selectivity indices of at least 0.71 were achieved even for  $\pm 10\%$  variations in the considered  $\partial E_x / \partial x$  threshold. Moreover, as we have considered only four *rotation angles* and discretized *y-offsets* with 1 mm intervals, a better selectivity could be possible for *rotation angles* and *y-offsets* that are not analyzed here. Although these results are for the rat sciatic nerve, the presented approaches can be easily extended to other multi-fascicular peripheral nerves found in other mammalian species.

## V. CONCLUSION

Peripheral nerve stimulation using magnetic coils can produce muscle responses similar to that of electrical stimulation and overcome some of the critical issues due to stimulation by electrodes. However, magnetic stimulation has limitations of high energy requirements and poor selectivity. In this work, we considered various configurations and orientations of figure-of-eight coils to optimize the required stimulation energy and improve the selectivity of peripheral nerve stimulation. We also studied how the number of turns and layers of a figure-of-eight coil affect the stimulation threshold for activation of nerve fibers. We found that a figure-of-eight coil configuration can reduce up to 50% of the stimulation voltage threshold, compared to a single cylindrical coil with the same number of turns and layers. Results suggest that the figure-of-eight coil with its two coils connected in a parallel connection requires less stimulation voltage to stimulate nerve fibers as compared to the corresponding series connection coil configuration. Similarly, the figure-of-eight coil configuration with opposite current flow directions generally provides a lower stimulation threshold than the coil configuration with the same current flow directions. By analyzing the number of turns and layers of the coil, we concluded that a very small or very large number of turns (or layers) leads to higher stimulation thresholds, and the lowest threshold is obtained for an optimal intermediate value of the number of turns (or layers). To attain selective stimulation, we considered coil orientations, with angles of  $0^\circ$ ,  $30^\circ$ ,  $60^\circ$ , and  $90^\circ$ , and coil translations in the perpendicular direction relative to the nerve in order to maximize stimulation selectivity. Using the optimized coil orientation, translation, and configuration, we could achieve an inter-fascicular selectivity with selectivity indices of 0.85 and 0.80 (or higher) for tibial and peroneal fascicles, respectively. Therefore, we conclude that reduction in stimulation threshold and selective stimulation of the peripheral nerve is possible by optimized design and orientation of the coil.

## REFERENCES

- [1] D. R. Merrill, M. Bikson, and J. G. R. Jefferys, "Electrical stimulation of excitable tissue: Design of efficacious and safe protocols," *J. Neurosci. Methods*, vol. 141, no. 2, pp. 171–198, Feb. 2005.
- [2] F. Lotti, F. Ranieri, G. Vadalá, L. Zollo, and G. Di Pino, "Invasive intraneural interfaces: Foreign body reaction issues," *Frontiers Neurosci.*, vol. 11, pp. 1–14, Sep. 2017.
- [3] T. Goroszeniuk and A. Król, "Peripheral neuromodulation: An update," *BOL*, vol. 18, no. 1, pp. 15–27, Jun. 2017.
- [4] K. Chakravarthy, A. Nava, P. J. Christo, and K. Williams, "Review of recent advances in peripheral nerve stimulation (PNS)," *Current Pain Headache Rep.*, vol. 20, no. 11, pp. 60–67, Nov. 2016.
- [5] P. M. Rossini *et al.*, "Non-invasive electrical and magnetic stimulation of the brain, spinal cord, roots and peripheral nerves: Basic principles and procedures for routine clinical and research application. An updated report from an I.F.C.N. committee," *Clin. Neurophysiol.*, vol. 126, no. 6, pp. 1071–1107, Jun. 2015.
- [6] J. Y. Shin, J.-H. Ahn, K. Pi, Y. S. Goo, and D.-I.-D. Cho, "Electrodeless, non-invasive stimulation of retinal neurons using time-varying magnetic fields," *IEEE Sensors J.*, vol. 16, no. 24, pp. 8832–8839, Dec. 2016.
- [7] S. Mukesh, D. T. Blake, B. J. McKinnon, and P. T. Bhatti, "Modeling intracochlear magnetic stimulation: A finite-element analysis," *IEEE Trans. Neural Syst. Rehabil. Eng.*, vol. 25, no. 8, pp. 1353–1362, Aug. 2017.
- [8] H.-J. Park, G. Bonmassar, J. A. Kaltenbach, A. G. Machado, N. F. Manzoor, and J. T. Gale, "Activation of the central nervous system induced by micro-magnetic stimulation," *Nature Commun.*, vol. 4, no. 1, pp. 2463–2481, Dec. 2013.
- [9] Z. B. Kagan, A. K. Ramrakhani, F. Khan, G. Lazzi, R. A. Normann, and D. J. Warren, "Magnetic stimulation of mammalian peripheral nerves *in vivo*: An alternative to functional electrical stimulation," in *Proc. 36th Annu. Int. Conf. IEEE Eng. Med. Biol. Soc.*, Aug. 2014, pp. 2573–2576.
- [10] S. Raspopovic, M. Capogrosso, and S. Micera, "A computational model for the stimulation of rat sciatic nerve using a transverse intrafascicular multichannel electrode," *IEEE Trans. Neural Syst. Rehabil. Eng.*, vol. 19, no. 4, pp. 333–344, Aug. 2011.
- [11] E. Basham, Z. Yang, and W. Liu, "Circuit and coil design for *in-vitro* magnetic neural stimulation systems," *IEEE Trans. Biomed. Circuits Syst.*, vol. 3, no. 5, pp. 321–331, Oct. 2009.
- [12] G. Bonmassar, S. W. Lee, D. K. Freeman, M. Polasek, S. I. Fried, and J. T. Gale, "Microscopic magnetic stimulation of neural tissue," *Nature Commun.*, vol. 3, no. 1, pp. 1–10, Jan. 2012.
- [13] H.-J. Park, H. Kang, J. Jo, E. Chung, and S. Kim, "Planar coil-based contact-mode magnetic stimulation: Synaptic responses in hippocampal slices and thermal considerations," *Sci. Rep.*, vol. 8, no. 1, pp. 1–10, Dec. 2018, doi: [10.1038/s41598-018-31536-w](https://doi.org/10.1038/s41598-018-31536-w).
- [14] P. J. Maccabee *et al.*, "Influence of pulse sequence, polarity and amplitude on magnetic stimulation of human and porcine peripheral nerve," *J. Physiol.*, vol. 513, no. 2, pp. 571–585, Dec. 1998.
- [15] S. M. Goetz, N. C. Truong, M. G. Gerhofer, A. V. Peterchev, H. Herzog, and T. Weyh, "Optimization of magnetic neurostimulation waveforms for minimum power loss," in *Proc. Annu. Int. Conf. IEEE Eng. Med. Biol. Soc.*, Aug. 2012, pp. 4652–4655.
- [16] S. M. Goetz, M. Pfäeffl, J. Huber, M. Singer, R. Marquardt, and T. Weyh, "Circuit topology and control principle for a first magnetic stimulator with fully controllable waveform," in *Proc. Annu. Int. Conf. IEEE Eng. Med. Biol. Soc.*, Aug. 2012, pp. 4700–4703.
- [17] S. M. Goetz, C. N. Truong, M. G. Gerhofer, A. V. Peterchev, H. G. Herzog, and T. Weyh, "Analysis and optimization of pulse dynamics for magnetic stimulation," *PLoS ONE*, vol. 8, no. 3, pp. 1–12, 2013.
- [18] L. Niehaus, B.-U. Meyer, and T. Weyh, "Influence of pulse configuration and direction of coil current on excitatory effects of magnetic motor cortex and nerve stimulation," *Clin. Neurophysiol.*, vol. 111, no. 1, pp. 75–80, Jan. 2000.
- [19] Z. B. Kagan, J. T. Mize, P. Kosta, G. Lazzi, R. A. Normann, and D. J. Warren, "Reduced heat generation during magnetic stimulation of rat sciatic nerve using current waveform truncation," *IEEE Trans. Neural Syst. Rehabil. Eng.*, vol. 27, no. 5, pp. 937–946, May 2019.
- [20] P. Kosta, D. J. Warren, and G. Lazzi, "Selective stimulation of rat sciatic nerve using an array of mm-size magnetic coils: A simulation study," *Healthcare Technol. Lett.*, vol. 6, no. 3, pp. 70–75, Jun. 2019.
- [21] P. J. Maccabee, L. Eberle, V. E. Amassian, R. Q. Cracco, and A. Rudell, "Studies of 3-dimensional voltage distributions induced in homogeneous media volume conductors by round and butterfly magnetic coils," in *Proc. Images 21st Century. Proc. Annu. Int. Eng. Med. Biol. Soc.*, 1989, pp. 1259–1260.
- [22] O. Hiwaki and S. Ueno, "Selective magnetic stimulation of the spinal cord," in *Proc. 12th Annu. Int. Conf. IEEE Eng. Med. Biol. Soc.*, Nov. 1990, pp. 436–437.



- [23] B. J. Roth *et al.*, "In vitro evaluation of a 4-leaf coil design for magnetic stimulation of peripheral nerve," *Electroencephalogr. Clin. Neurophysiol./Evoked Potentials Sect.*, vol. 93, no. 1, pp. 68–74, Feb. 1994.
- [24] K.-H. Hsu and D. M. Durand, "A 3-D differential coil design for localized magnetic stimulation," *IEEE Trans. Biomed. Eng.*, vol. 48, no. 10, pp. 1162–1168, 2001.
- [25] C. Ren, P. P. Tarjan, and D. B. Popovic, "A novel electric design for electromagnetic stimulation—The slinky coil," *IEEE Trans. Biomed. Eng.*, vol. 42, no. 9, pp. 918–925, 1995.
- [26] Y. Roth, A. Zangen, and M. Hallett, "A coil design for transcranial magnetic stimulation of deep brain regions," *J. Clin. Neurophysiol.*, vol. 19, no. 4, pp. 361–370, Aug. 2002.
- [27] V. W.-H. Lin, I. N. Hsiao, and V. Dhaka, "Magnetic coil design considerations for functional magnetic stimulation," *IEEE Trans. Biomed. Eng.*, vol. 47, no. 5, pp. 600–610, May 2000.
- [28] N. Al-Mutawaly and R. D. Findlay, "A novel coil design for magnetic nerve stimulation," in *Proc. Conf. IEEE Can. Conf. Electr. Comput. Eng.*, May 1998, pp. 669–672.
- [29] N. Al-Mutawaly, H. de Bruin, and D. Findlay, "Magnetic nerve stimulation: Field focality and depth of penetration," in *Proc. Conf. Proc. 23rd Annu. Int. Conf. IEEE Eng. Med. Biol. Soc.*, vol. 1, Oct. 2001, pp. 877–880.
- [30] S. W. Lee, F. Fallegger, B. D. F. Casse, and S. I. Fried, "Implantable microcoils for intracortical magnetic stimulation," *Sci. Adv.*, vol. 2, no. 12, Dec. 2016, Art. no. e1600889.
- [31] Z. D. Deng, S. H. Lisanby, and A. V. Peterchev, "Electric field depth-focality tradeoff in transcranial magnetic stimulation: Simulation comparison of 50 coil designs," *Brain Stimulation*, vol. 6, no. 1, pp. 1–13, 2013.
- [32] S. M. Goetz, T. Weyh, I. A. Afinowi, and H.-G. Herzog, "Coil design for neuromuscular magnetic stimulation based on a detailed 3-d thigh model," *IEEE Trans. Magn.*, vol. 50, no. 6, pp. 1–10, Jan. 2014.
- [33] S. M. Goetz, H. G. Herzog, N. Gatteringer, and B. Gleich, "Comparison of coil designs for peripheral magnetic muscle stimulation," *J. Neural Eng.*, vol. 8, no. 5, pp. 1–8, 2011.
- [34] L. G. Cohen *et al.*, "Effects of coil design on delivery of focal magnetic stimulation. Technical considerations," *Electroencephalogr. Clin. Neurophysiol.*, vol. 15, no. 12, pp. 12–14, 1990.
- [35] A. Thielscher and T. Kammer, "Electric field properties of two commercial figure-8 coils in TMS: Calculation of focality and efficiency," *Clin. Neurophysiol.*, vol. 115, no. 7, pp. 1697–1708, Jul. 2004.
- [36] A. G. Guggisberg, P. Dubach, C. W. Hess, C. Wüthrich, and J. Mathis, "Motor evoked potentials from masseter muscle induced by transcranial magnetic stimulation of the pyramidal tract: The importance of coil orientation," *Clin. Neurophysiol.*, vol. 112, no. 12, pp. 2312–2319, Dec. 2001.
- [37] K. R. Mills, S. J. Boniface, and M. Schubert, "Magnetic brain stimulation with a double coil: The importance of coil orientation," *Electroencephalogr. Clin. Neurophysiol./Evoked Potentials Sect.*, vol. 85, no. 1, pp. 17–21, Feb. 1992.
- [38] P. Adank, D. Kennedy-Higgins, G. Maegherman, R. Hannah, and H. E. Nuttall, "Effects of coil orientation on motor evoked potentials from orbicularis oris," *Frontiers Neurosci.*, vol. 12, pp. 1–8, Nov. 2018.
- [39] P. Dubach, A. G. Guggisberg, K. M. Rösler, C. W. Hess, and J. Mathis, "Significance of coil orientation for motor evoked potentials from nasalis muscle elicited by transcranial magnetic stimulation," *Clin. Neurophysiol.*, vol. 115, no. 4, pp. 862–870, Apr. 2004.
- [40] R. H. Thomson *et al.*, "Blood oxygenation changes modulated by coil orientation during prefrontal transcranial magnetic stimulation," *Brain Stimulation*, vol. 6, no. 4, pp. 576–581, Jul. 2013.
- [41] J. Ruohonen, J. Virtanen, and R. J. Ilmoniemi, "Coil optimization for magnetic brain stimulation," *Ann. Biomed. Eng.*, vol. 25, no. 5, pp. 840–849, Sep. 1997.
- [42] J. Ruohonen, P. Ravazzani, and F. Grandori, "Functional magnetic stimulation: Theory and coil optimization," *Bioelectrochemistry Bioenergetics*, vol. 47, no. 2, pp. 213–219, Dec. 1998.
- [43] J. Mathis, "The boundary effect in magnetic stimulation. Analysis at the peripheral nerve," *Electroencephalogr. Clin. Neurophysiol.*, vol. 97, no. 5, pp. 238–245, Oct. 1995.
- [44] M. Ravnborg, M. Blinkenberg, and K. Dahl, "Significance of magnetic coil position in peripheral motor nerve stimulation," *Muscle Nerve*, vol. 13, no. 8, pp. 681–686, Aug. 1990.
- [45] S. S. Nagarajan, D. M. Durand, and K. Hsuing-Hsu, "Mapping location of excitation during magnetic stimulation: Effects of coil position," *Ann. Biomed. Eng.*, vol. 25, no. 1, pp. 112–125, Jan. 1997.
- [46] J. Nilsson *et al.*, "Determining the site of stimulation during magnetic stimulation of a peripheral nerve," *Electroencephalogr. Clin. Neurophysiol./Evoked Potentials Sect.*, vol. 85, no. 4, pp. 253–264, Aug. 1992.
- [47] J. Ruohonen, M. Panizza, J. Nilsson, P. Ravazzani, F. Grandori, and G. Tognola, "Transverse-field activation mechanism in magnetic stimulation of peripheral nerves," *Electroencephalogr. Clin. Neurophysiol./Electromyography Motor Control*, vol. 101, no. 2, pp. 167–174, Apr. 1996.
- [48] S.-J. Sun, S. Tobimatsu, and M. Kato, "The effect of magnetic coil orientation on the excitation of the median nerve," *Acta Neurologica Scandinavica*, vol. 97, no. 5, pp. 328–335, May 1998.
- [49] O. Kiwaki and H. Kuwano, "Properties of peripheral nerve excitation in respect of location of coil for magnetic nerve stimulation," in *Proc. Conf. 23rd Annu. Int. Conf. IEEE Eng. Med. Biol. Soc.*, Oct. 2001, pp. 892–895.
- [50] A. K. Ramrakhiani, Z. B. Kagan, D. J. Warren, R. A. Normann, and G. Lazzi, "A  $\mu$ m-scale computational model of magnetic neural stimulation in multifascicular peripheral nerves," *IEEE Trans. Biomed. Eng.*, vol. 62, no. 12, pp. 2837–2849, Dec. 2015.
- [51] M. L. Hines and N. T. Carnevale, "The NEURON simulation environment," *Neural Comput.*, vol. 9, no. 6, pp. 1179–1209, Aug. 1997.
- [52] B. J. Roth and P. J. Basser, "A model of the stimulation of a nerve fiber by electromagnetic induction," *IEEE Trans. Biomed. Eng.*, vol. 37, no. 6, pp. 588–597, Jun. 1990.
- [53] P. J. Basser and B. J. Roth, "Stimulation of a myelinated nerve axon by electromagnetic induction," *Med. Biol. Eng. Comput.*, vol. 29, no. 3, pp. 261–268, May 1991.
- [54] T. Pashut *et al.*, "Mechanisms of magnetic stimulation of central nervous system neurons," *PLoS Comput. Biol.*, vol. 7, no. 3, Mar. 2011, Art. no. e1002022.
- [55] B. J. Roth, L. G. Cohen, M. Hallett, W. Friauf, and P. J. Basser, "A theoretical calculation of the electric field induced by magnetic stimulation of a peripheral nerve," *Muscle Nerve*, vol. 13, no. 8, pp. 734–741, Aug. 1990.
- [56] M. B. Christensen and P. A. Tresco, "Differences exist in the left and right sciatic nerves of Naïve rats and cats," *Anatomical Rec.*, vol. 298, pp. 1492–1501, Aug. 2015.
- [57] J. W. Moore, R. W. Joyner, M. H. Brill, S. D. Waxman, and M. Najar-Joa, "Simulations of conduction in uniform myelinated fibers. Relative sensitivity to changes in nodal and internodal parameters," *Biophysical J.*, vol. 21, no. 2, pp. 147–160, Feb. 1978.
- [58] M. H. Brill, S. G. Waxman, J. W. Moore, and R. W. Joyner, "Conduction velocity and spike configuration in myelinated fibres: Computed dependence on internode distance," *J. Neurol., Neurosurgery Psychiatry*, vol. 40, no. 8, pp. 769–774, Aug. 1977.
- [59] B. Frankenhaeuser and A. Huxley, "The action potential in the myelinated nerve fibre of xenopus laevis as computed on the basis of voltage clamp data," *J. Physiol.*, vol. 171, no. 2, p. 302, 1964.
- [60] J. R. Schwarz and G. Eikhof, "Na currents and action potentials in rat myelinated nerve fibres at 20 and 37°C," *Pflügers Archiv-Eur. J. Physiol.*, vol. 409, no. 6, pp. 569–577, Aug. 1987.
- [61] C. C. McIntyre, A. G. Richardson, and W. M. Grill, "Modeling the excitability of mammalian nerve fibers: Influence of afterpotentials on the recovery cycle," *J. Neurophysiol.*, vol. 87, no. 2, pp. 995–1006, Feb. 2002.
- [62] M. A. Latorre and K. Wårdell, "A comparison between single and double cable neuron models applicable to deep brain stimulation," *Biomed. Phys. Eng. Express*, vol. 5, no. 2, Jan. 2019, Art. no. 025026.
- [63] N. Orcutt and O. P. Gandhi, "A 3-D impedance method to calculate power deposition in biological bodies subjected to time varying magnetic fields," *IEEE Trans. Biomed. Eng.*, vol. 35, no. 8, pp. 577–583, Aug. 1988.
- [64] C. R. Butson, I. O. Miller, R. A. Normann, and G. A. Clark, "Selective neural activation in a histologically derived model of peripheral nerve," *J. Neural Eng.*, vol. 8, no. 3, Jun. 2011, Art. no. 036009.
- [65] Z. B. Kagan, A. K. Ramrakhiani, G. Lazzi, R. A. Normann, and D. J. Warren, "In vivo magnetic stimulation of rat sciatic nerve with Centimeter- and millimeter-scale solenoid coils," *IEEE Trans. Neural Syst. Rehabil. Eng.*, vol. 24, no. 11, pp. 1138–1147, Nov. 2016.
- [66] A. K. Ramrakhiani and G. Lazzi, "Ferrite core non-linearity in coils for magnetic neurostimulation," *Healthcare Technol. Lett.*, vol. 1, no. 4, pp. 87–91, Oct. 2014.
- [67] E. Basham, Z. Yang, N. Tchemodanov, and W. Liu, "Magnetic stimulation of neural tissue: Techniques and system design," in *Implantable Neural Prostheses 1: Devices and Applications*. New York, NY, USA: Springer, 2009, pp. 293–351.